Research Square

Preprints are preliminary reports that have not undergone peer review.
They should not be considered conclusive, used to inform clinical practice,
or referenced by the media as validated information.

Ultrahigh energy storage performance in $Pb_{0.94}La_{0.04}Zr_{0.99}Ti_{0.01}O_3$ ceramics via introducing pyrochlore phase $Y_2Zr_2O_7$

Lei Cao
Inner Mongolia University of Science and Technology
Bowen Huang
Inner Mongolia University of Science and Technology
Tianci Yang
Inner Mongolia University of Science and Technology
Chenglong Jiang
Inner Mongolia University of Science and Technology
Ye Zhao
yzhao@imust.edu.cn
Inner Mongolia University of Science and Technology
Pei Han
Inner Mongolia University of Science and Technology
Rong Ma
Inner Mongolia University of Science and Technology
Chunxiao Lu
Inner Mongolia University of Science and Technology
Fen Zhao
Baotou Zhongke Investment Management
Liwen Zhang
Inner Mongolia University of Science and Technology
Yong Li
Inner Mongolia University of Science and Technology

Research Article

Keywords: Antiferroelectric, Energy storage performances, Dual-phase composite ceramics, Y2O3, Breakdown strength

Posted Date: April 20th, 2026

DOI: https://doi.org/10.21203/rs.3.rs-9095268/v1

License: This work is licensed under a Creative Commons Attribution 4.0 International License.
Read Full License

Additional Declarations: No competing interests reported.

Abstract

Antiferroelectric (AFE) ceramics hold great promise for high energy density capacitors, though their energy storage properties (ESPs) are fundamentally limited by a relatively low breakdown electric field (E_b). Hence, the dual-phase composite ceramics were designed by incorporating a pyrochlore phase into the perovskite matrix to enhance ESPs. Composite ceramics of $Y_2Zr_2O_7$ modified $Pb_{0.94}La_{0.04}Zr_{0.99}Ti_{0.01}O_3$- *x* wt% Y_2O_3 were fabricated and investigated. The introduction of $Y_2Zr_2O_7$ serves to reduce the overall dielectric permittivity (ε_r) and enhance insulation, which collectively raise the E_b from 420 kV/cm to 850 kV/cm. A maximum recoverable energy density (W_{rec}) of 14.5 J/cm^3 with an energy efficiency (η) of 85.7% are achieved in the ceramic with *x* = 4 under 570 kV/cm. In addition, a current density (C_D) as high as 2369.4 A/cm^2, a power density (P_D) of 462 MW/cm^3, and an ultrafast discharge rate of 22.6 ns are achieved. This work establishes the construction of dual-phase composites as a viable and novel approach to improving ESPs in $PbZrO_3$ (PZ) -based ceramic systems.

1. Introduction

Ceramic capacitors exhibit broad application prospects in electric vehicles, pulse power systems, and other fields due to their excellent charge-discharge rates and high power density (P_D)[1–3]. However, the relatively low energy storage density remains a key bottleneck limiting their miniaturization and integration. Therefore, improving energy storage properties (ESPs) is of significant scientific importance and practical value. In general, the total energy storage density (W_{tot}), recoverable energy storage density (W_{rec}) and energy storage efficiency (η) of dielectric ceramic capacitors can be calculated using the following formulas[4]:

$$\mathrm{W_{tot}}=\int_0^{\mathrm{P_{max}}}\mathrm{EdP}\#\,(1)$$

$$\mathrm{W_{rec}}=\int_{\mathrm{P_r}}^{\mathrm{P_{max}}}\mathrm{EdP}\#\,(2)$$

$$\eta=\frac{\mathrm{W_{rec}}}{\mathrm{W_{tot}}}\times 100\%\#\,(3)$$

where *E*, P_r, and P_{max} denote as the applied electric field, remanent polarization, and maximum polarization, respectively. The formulas reveal that achieving a high W_{rec} necessitates concurrently high P_{max}, low P_r and high breakdown field (E_b). Among these, pursuing E_b optimization emerges as a particularly effective strategy, as the improvement from polarization enhancement alone is intrinsically constrained[5].

$PbZrO_3$ (PZ) -based antiferroelectric (AFE) ceramics are considered one of the most promising energy storage dielectric ceramics for achieving high W_{rec} due to their unique double hysteresis loops and high P_{max} and near-zero P_r[6]. The ESPs of PZ-based AFE materials are primarily constrained by their low E_b. Consequently, rare-earth ion doping has been widely adopted as a feasible strategy to enhance E_b and

thereby improve ESPs[7]. For example, Yang et al. demonstrated that Nd^{3+} doping stabilized the AFE phase in a $Pb_{0.98}Sr_{0.02}Zr_{0.75}Sn_{0.25}O_3$ (PSrZS) ceramics, increasing its E_b from 350 kV/cm to 540 kV/cm and resulting in a high W_{rec} of 14.21 J/cm^3 with η of 87.35%[8]. In addition to ion doping, constructing dual-phase composite ceramics is also an effective strategy to improve the breakdown characteristics of dielectric ceramics[9]. For example, Pan et al. introduced the pyrochlore $Sm_2Sn_2O_7$ into a $Bi_{0.5}Na_{0.5}TiO_3$ (BNT) -based perovskite matrix, raising the E_b from 220 to 700 kV/cm and achieving a W_{rec} of 9.91 J/cm^3 with η of 87.01%[10]. Such enhanced ESPs are attributed to the existence of pyrochlore phase in perovskite matrix, which possesses a low dielectric constant (ε_r), wide bandgap (E_g), low dielectric loss (tanδ), and high stability[11–13]. Therefore, constructing a composite structure by introducing a pyrochlore phase ($Y_2Zr_2O_7$) into perovskite dielectric ceramics is a promising strategy to significantly enhance ESPs, offering broad application prospects.

$Y_2Zr_2O_7$ is a pyrochlore phase transparent ceramic with a low ε_r (~ 27), wide E_g (~ 4.5 eV), low tanδ (~ 0.001), and high thermal resistance (1.2 ~ 1.3 W/(m·k)). While currently utilized mainly in phosphors and photochromism applications, distinctive dielectric properties also render it a promising candidate for energy storage applications[14–18]. Previous studies indicate that doping Y^{3+} into the A-site can induce local chemical disorder, disrupt the original long-range ferroelectric order of the PZ-based ceramics, and promote a transition to a diffuse relaxor state. Simultaneously, it helps to reduce oxygen vacancy concentration, refine grain size, and enhance E_b[19]. In this work, a series of $Pb_{0.94}La_{0.04}Zr_{0.99}Ti_{0.01}O_3$ (PLZT) - x wt% Y_2O_3 ceramics were designed by introducing x wt% Y_2O_3 at the initial mixing stage. This non-equivalent doping strategy promotes the directional formation of a secondary phase within the PLZT matrix. Consequently, it enhances the stability of the AFE state and simultaneously improves the E_b, leading to excellent overall ESPs. This work offers a promising composite ceramic candidate for pulsed power systems.

2. Experimental Section

Antiferroelectric ceramics with the composition of $Pb_{0.94}La_{0.04}Zr_{0.99}Ti_{0.01}O_3$- x wt%Y_2O_3 with x = 0, 2, 4, 6, and 8 were prepared by a tape-casting. These samples are accordingly designated as Y0, Y2, Y4, Y6 and Y8. The starting materials are lead tetroxide (Pb_3O_4, 95.0%), yttrium oxide (Y_2O_3, 99.9%), zirconium dioxide (ZrO_2, 99.0%), titanium dioxide (TiO_2, 99.5%), lanthanum oxide (La_2O_3, 99.9%). PLZT ($Pb_{0.94}La_{0.04}Zr_{0.99}Ti_{0.01}O_3$) were weighed according to the stoichiometric ratio, but yttrium oxide is doped in proportion to the mass of the corresponding powder. All raw materials ball milled in alcohol for 24 h. The mixture was calcined at 900 ^oC for 2 h, followed by grinding and a second 24 h ball-milling. After drying and sieving, the powder was shaped via tape-casting, subsequently air-dried, and densified through sequential hot pressing and cold isostatic pressing. Organic components were removed at 600 ^oC for 5 h. The samples were sintered at 1160 ^oC for 3 h, polished to a thickness of ~ 70 μm, and coated with 1 mm-diameter gold electrodes via ion suppering for electrical properties.

The crystal structure was characterized using X-ray diffraction (XRD; Bruker D8 Advance) with Cu K*α* radiation. The obtained diffraction patterns were refined using the Rietveld method in GSAS-II software. Microstructure analysis was conducted using a scanning electron microscope (SEM; Thermo Fisher MIRA3) operated in backscattered electron (BSE) mode. The impedance spectrum was measured using an impedance analyzer (Agilent E4990A). The polarization-electric field (*P-E*) hysteresis loops and current-electric field (*I-E*) curve loops were measured using a ferroelectric testing system integrated with a temperature-controlled probe station (Radiant Technologies) at 10 Hz. The charge-discharge performance was evaluated using a dedicated pulse power platform (Gogo Instruments CFD137005) connected to a DC power supply (ENTAI ET2671A).

3. Results and Discussion

Figure 2(a) presents the XRD pattern of the PLZT- *x* wt% Y_2O_3 ceramic. The main crystalline phase corresponds to a typical perovskite structure (PDF# 97-016-6843) with an orthorhombic symmetry. With increasing Y_2O_3 content, diffraction peaks corresponding to the cubic pyrochlore phase $Y_2Zr_2O_7$ (PDF# 97-015-3818) gradually emerge, and their intensities progressively increase. The results indicate that excessive Y_2O_3 doping exceeds the solid solubility limit in the PLZT matrix, leading to the precipitation of the secondary phase[20]. To quantify the relative content of the perovskite and pyrochlore phases, the Rietveld refinement was conducted. As shown in Fig. 2(b), the Rietveld refinement results of Y0 and Y4 ceramics indicate that all samples exhibit a typical perovskite structure, and the content of pyrochlore phase monotonically increases with the increase of Y^{3+} content. The refinement was carried out simultaneously based on two spatial group models: orthorhombic phase Pba2 and cubic phase Fd-3m. All the samples exhibit low *R*-factors (R_{wp} < 10%), and unit cell parameters for Y4 ceramics are provided in **Fig. S1.** These results confirm the validity of the structural models and the reliability of the refinement, with the calculated patterns showing excellent agreement with the experimental data[21]. The XRD Rietveld refinement patterns for ceramics Y2, Y6 and Y8 are provided in **Fig. S2.** It can be seen that the formation of the $Y_2Zr_2O_7$ pyrochlore phase increases the cubic phase fraction to 8.8% in Y2 sample. With further increase in Y_2O_3 addition, it reaches 48% in Y4 and eventually rises nonlinearly to 60.4% in Y8 (Fig. 2(c)). This evolution is attributed to the limited solubility of Y_2O_3 in the PLZT lattice. This limited solubility disrupts the long-range ferroelectric order, thereby enhancing the relaxor behavior of the materials [22].

To further elucidate the influence of Y_2O_3 on the structural characteristics, room-temperature Raman spectra were collected (**Fig. S3**). A detailed Gaussian-Lorentzian fitting analysis was conducted on the Raman spectra of the Y0 and Y4 samples, as shown in Fig. 2(d). The spectral features are systematically divided into three distinct regions: A-site ion vibrations (50 ~ 150 cm^{-1}), B-O bond vibrations (150 ~ 450 cm^{-1}), and BO_6 octahedral vibrations (450 ~ 800 cm^{-1}). The Y4 sample exhibits significant spectral alterations in the low-frequency region (< 150 cm^{-1}) compared to Y0, resulting from the perturbation of A-site vibrational modes by Y^{3+} doping. Concurrently, the Raman peak near 220 cm^{-1} shifts in position

and exhibits a reduced full width at half maximum (FWHM), indicating enhanced lattice distortion [23]. Furthermore, in the region of 450 ~ 800 cm^{-1}, the absence of a characteristic J-fitting peak in Y4 sample suggests that the precipitation of the secondary phase enhances the structural stability of the BO_6 octahedra.

As shown in Fig. 2(e) and (f), both Y0 and Y4 ceramics exhibit well-defined grain with sharp boundaries and a dense microstructure, indicating the suitability of the sintering temperature. The BSE images (Fig. 2(f)) reveal the stable coexistence of pyrochlore phase $Y_2Zr_2O_7$ and perovskite phase PLZT in the Y4 ceramic, which has been consistently reproduced in repeated experiments. This indicates that the significant enhancement in E_b is not due to grain size effects[22]. To identify the composition of the second phase, energy-dispersive X-ray spectroscopy (EDS) was conducted on all samples, as shown in **Fig. S4**. The results demonstrate a distinct co-enrichment of Y^{3+} and Zr^{4+} ions in Y4 samples, confirming the formation of the $Y_2Zr_2O_7$ secondary phase[23].

The breakdown reliability was evaluated using Weibull distribution analysis, as shown in Fig. 3(a). All the PLZT- *x* wt% Y_2O_3 ceramics exhibit a Weibull modulus (β) higher than 10, indicating excellent consistency and high reliability of the E_b[24]. The E_b of Y0, Y2, Y4, Y6, and Y8 ceramics are 440 kV/cm, 490 kV/cm, 570 kV/cm, 720 kV/cm, and 850 kV/cm, respectively. The current-voltage (I-V) characteristics of all samples (Fig. S4) reveal consistently low leakage currents across the measured bias range. In addition, according to previous studies, modifications in the band structure contribute to the enhancement of E_b[25]. To further elucidate the underlying mechanism for the improved E_b, UV-Vis spectroscopy was conducted (Fig. 3(b)). The optical E_g increases from 2.65 eV for Y0 to 2.73 eV for Y4, indicating that charge carrier migration must overcome a higher energy barrier. This widening of the E_g raises the activation energy for carrier transport, effectively suppressing electrical conduction and allowing the ceramic to withstand higher applied electric fields, thereby leading to superior ESPs[26]. Figure 3(c) shows the impedance spectra, revealing that the Y4 ceramics has a significantly higher total resistance than Y0 ceramics. The Y0 ceramics exhibits two capacitive arcs, corresponding to grains and grain boundaries responses, whereas the Y4 ceramics displays a single capacitive arc[27]. This behavior results from the formation of a high-resistance pyrochlore phase in the Y4 ceramics. The resistance of this phase exceeds the combined resistance of the grains and grain boundaries of Y0 ceramics, thereby dominating the overall impedance response [28]. To elucidate the intrinsic correlation between the dielectric breakdown behavior and the composite microstructure of PLZT- *x* wt% Y_2O_3 ceramics, phase-field simulations were conducted [21, 24–26, 29, 30].The experimentally measured SEM grain morphology from Fig. 3(d) and (f) was used as the input microstructure for the phase simulations. In contrast to the single-pole concentration of electric potential in the pure perovskite Y0 ceramics (Fig. 3(e)). When the breakdown path encounters the $Y_2Zr_2O_7$ grains, it hinders the electrical breakdown process (Fig. 3(f)). This uniform distribution originates from the dual-phase grains characterized by low ε_r and weak polarization. These features effectively impede the propagation of conductive pathways and suppress the localization of high electric fields. Consequently, under identical voltage conditions, the Y4

ceramics exhibits superior breakdown resistance, and reduced susceptibility to failure, thereby achieving a higher E_b[31, 32].

The dielectric temperature spectra of PLZT-*x* wt% Y_2O_3 ceramics measured at 100 kHz are presented in Fig. 4(a). All compositions exhibit distinct dielectric peaks. With increasing Y_2O_3 content, the dielectric response evolves from three well-defined peaks in the Y0 ceramics to a single broadened peak[33], which is observed across the Y2 to Y8 ceramics. The progressive broadening of the dielectric peaks reflects characteristic diffuse phase transition behavior, which can be attributed to enhanced ionic disorder resulting from the random distribution of cations within the solid solution[34]. At elevated temperatures, the tanδ of PLZT-*x* wt% Y_2O_3 ceramics shows a marked decrease. This improvement is likely due to the enhanced high-temperature stability and the reduced high-temperature dielectric loss of the matrix imparted by the secondary phase [35]. The *P-E* loops characteristics of PLZT-*x* wt% Y_2O_3 ceramics under 400 kV/cm are shown in Fig. 4(b). A marked decrease in the polarization intensity of PLZT-*x* wt% Y_2O_3 ceramics can be observed, and the reduction is similar to the proportional increase of the second phase. For example, the P_{max} values of Y0, Y2, Y4, Y6, and Y8 ceramics are 52.7 C/cm^2, 40.8 C/cm^2, 25.2 μC/cm^2, 15.9 μC/cm^2, and 14.8 μC/cm^2 under 400 kV/cm, respectively. Therefore, the decrease in P_{max} can be attributed to the incorporation of the cubic $Y_2Zr_2O_7$ phase, which possesses a highly symmetric structure and exhibits neither FE nor AFE ordering, thus contributing no spontaneous polarization. Furthermore, in Fig. 4(c), the current peak in the *I-E* loops shifts toward higher electric fields, accompanied by a decrease in dielectric peak intensity and a broadening of peak width. These changes indicate that increasing the $Y_2Zr_2O_7$ content modulates the phase behavior, suppresses intense strain generation, and delays polarization saturation [36]. Figure 4(d) and (e) present the *P-E* loops and ESPs of PLZT-*x* wt% Y_2O_3 ceramics. This improvement arises from the synergistic effect between enhanced relaxation behavior and increased E_b, resulting in a high W_{rec} of 14.5 J/cm^3 and an η of 85.7%. A comparative analysis with other ceramics systems (Fig. 4(f)) confirms the superior overall ESPs of Y4 ceramics, further supported by a comprehensive evaluation of its efficiency and ESPs [1, 3–6, 9, 19, 20, 37, 38].

For dielectric ceramic capacitors, the ability to withstand harsh operating conditions is critically important in practical applications. The temperature, frequency, and cycling stability of the Y4 ceramics were systematically evaluated through *P-E* loops measurements, as shown in Fig. 5(a) ~ (c). It can be seen that the Y4 ceramics exhibits pronounced temperature dependence over the range from 30 ^oC to 150 ^oC. With increasing temperature, this accumulated thermal energy facilitates electric domain switching, promoting the AFE-to-FE phase transition and resulting in a continuous rise in P_{max} from 19.4 μC/cm^2 (30 ^oC) to 31.4 μC/cm^2 (150 ^oC). Accordingly, the W_{rec} increases from 5.03 J/cm^3 at 30 ^oC to 7.61 J/cm^3 at 120 ^oC (Fig. 5(d)). This demonstrates that Y4 ceramic can deliver enhanced ESPs at elevated temperatures (90–150 ^oC). The Y4 ceramics also exhibits excellent stability over a broad frequency range from 1 Hz to 1000 Hz, with only an 8% variation in its W_{rec}, as shown in Fig. 5(e). The ESPs remains highly stable, which is a critical advantage for high-frequency pulse power systems. To

assess the cycling stability of the Y4 ceramics, Fig. 5 (f) presents the evolution of the W_{rec} and η calculated by *P-E* loops after 10^4 cycles under an applied electric field of 300 kV/cm. The Y4 ceramic exhibits excellent cycling stability after 10^4 cycles with 12.6% variation in W_{rec}.

To assess its viability for pulsed power systems, the charge-discharge performance of the Y4 ceramics was investigated. Room-temperature tests were conducted under overdamped (200 Ω) and underdamped circuit conditions. As shown in Fig. 6(a) and (b), the underdamped discharge current increases with the applied electric field. The maximum current (I_{max}) of 18.6 A, current density ($C_D = I_{max} / S$) of 2369.4 A/cm^2, and a power density ($P_D = E \times I_{max} / S$) of 462 MW/cm^3 are achieved in the Y4 ceramic at 390 kV/cm. Meanwhile, the overdamped discharge curves in Fig. 6(c) and (d) demonstrate an exceptionally rapid energy release. The discharge speed is quantified by $t_{0.9}$, the time to release 90% of the total discharge energy density (W_{dis}), calculated as follows:[39–42]:

$$\mathrm{W_{dis}} = \frac{\mathrm{R}\int \mathrm{i}^2(\mathrm{t})\mathrm{dt}}{\mathrm{V}} \# (4)$$

where *V* represents sample volume, and *R* represents load resistance (200 Ω). It can be seen that the W_{dis} is 2.14 J/cm^3 at 430 kV/cm, and a fast discharge time of $t_{0.9}$ = 22.6 ns is obtained in Y4 ceramic. These results indicate that rare earth-modified PLZT ceramics possess outstanding ESPs, positioning them as a competitive candidate for pulsed powerapplications.

4. Conclusion

This work successfully developed a $Pb_{0.94}La_{0.04}Zr_{0.99}Ti_{0.01}O_3$- *x* wt% Y_2O_3 (PLZT- *x* wt% Y_2O_3) composite ceramics for dielectric energy storage. Increasing the Y_2O_3 content *x* systematically enhances the E_b of the PLZT matrix and promotes the evolution toward a two-phase heterostructure composed of perovskite (PLZT) and pyrochlore ($Y_2Zr_2O_7$) phases. Y4 ceramic achieves a large W_{rec} of 14.5 J/cm^3 under a high E_b of 570 kV/cm, together with excellent stability over a wide frequency range (1 ~ 1000 Hz) and more than 10^4 charge-discharge cycles. It also delivers a high P_D of 462 MW/cm^3, a large C_D of 2369.4 C/cm^2, and an ultrafast discharge response ($t_{0.9}$ = 22.6 ns). The rationally designed dual-phase heterostructure in Y4 ceramics enables exceptional integrated performance for pulsed-power systems, thereby paving the way for a new design paradigm in high-performance energy-storage ceramics.

Declarations

Declaration of competing interest

The authors declare that they have no known competing financial interests or personal relationships that could have appeared to influence the work reported in this paper.

Author Contribution

Lei Cao: conceptualization, investigation, validation, methodology, writing - original draft. Ye Zhao: methodology, conceptualization, writing - reviewing and editing, project administration. Bowen Huang: investigation, formal analysis. Tianci Yang: investigation, formal analysis. Chenglong Jiang: investigation, formal analysis. Pei Han: investigation, formal analysis, writing - reviewing and editing. Rong Ma: investigation, formal analysis. Chunxiao Lu: investigation, formal analysis. Fen Zhao: investigation, formal analysis. Liwen Zhang: investigation, formal analysis. Yong Li: methodology, conceptualization, project administration.

Acknowledgements

This work was supported by the Scientific and Technological Development Foundation of the Central Guidance Local (2025ZY0168), the Natural Science Foundation of Inner Mongolia Autonomous Region (2024MS05024, 2024MS05016, 2024FX14), the Innovation Platform Construction Plan in the Inner Mongolia Autonomous Region (2025KYPT0129), and First-Class Discipline Research Special Project (YLXKZX-NKD-042).

Data Availability

The data that support the findings of this study are available from the corresponding author upon reasonable request.

References

1. P.-Z. Ge, X.-G. Tang, K. Meng, X.-X. Huang, S.-F. Li, Q.-X. Liu, Y.-P. Jiang, Energy storage density and charge-discharge properties of $Pb_xHf_{1-x}SnO_3$ antiferroelectric ceramics. Chem. Eng. J. **429**, 132540 (2022). http://dx.doi.org/10.1016/j.cej.2021.132540
2. J. Liu, Q. Chai, C. Yang, Y. Wang, Z. Peng, X. Chao, Z. Yang, Ultrahigh energy storage density and high energy efficiency in $K_{0.5}Na_{0.5}NbO_3$-based ceramics under moderate electric fields via multiple synergistic optimization. Chem. Eng. J. **525**, 170432 (2025). http://dx.doi.org/10.1016/j.cej.2025.170432
3. Y. Zheng, Z. Dai, C. Liu, Q. Guo, X. Zhao, S. Tsukada, Y. Cong, S. Gu, T. Karaki, Improvement of energy storage properties of $Bi_{0.5}Na_{0.5}TiO_3$ ceramics by doping $La_{0.9}Bi_{0.1}Ni_{0.67}Ta_{0.33}O_3$. Ceram. Int. **51**(16), 22247–22254 (2025). http://dx.doi.org/10.1016/j.ceramint.2025.02.386
4. Z. Lv, B. Han, Z. Liu, S. Guo, K. Dai, F. Cao, Z. Hu, G. Wang, Achieving excellent energy storage properties in lead-free ceramics via competing FE/AFE phase coexistence. Energy Storage Mater. **77**, 104205 (2025). http://dx.doi.org/10.1016/j.ensm.2025.104205

5. Y. Xu, Z. Yang, K. Xu, Y. Cao, Y. Tian, L. Guo, J. Tian, H. Tian, X. Liu, L. Lin, G. Wang, Modulated band structure and phase transitions in calcium hafnate titanate modified silver niobate ceramics for energy storage. Chem. Eng. J. 426 (2021). http://dx.doi.org/10.1016/j.cej.2021.131047
6. J. Zhou, Z. Xu, H. Yang, L. Chu, L. Chen, H. Li, J. Ding, S. Ran, Z. Sun, X. Hao, Excellent energy storage performance of lead-based antiferroelectric ceramics via enhancing dielectric breakdown mechanism. Chem. Eng. J. 487 (2024). http://dx.doi.org/10.1016/j.cej.2024.150476
7. J. Jiang, X. Meng, L. Li, S. Guo, M. Huang, J. Zhang, J. Wang, X. Hao, H. Zhu, S.-T. Zhang, Ultrahigh energy storage density in lead-free relaxor antiferroelectric ceramics via domain engineering. Energy Storage Mater. **43**, 383–390 (2021). http://dx.doi.org/10.1016/j.ensm.2021.09.018
8. J. Yang, G. Ge, C. Chen, B. Shen, J. Zhai, X. Chou, Field-induced strain engineering to optimize antiferroelectric ceramics in breakdown strength and energy storage performance. Acta Mater. **257** (2023). http://dx.doi.org/10.1016/j.actamat.2023.119186
9. C. Wu, Y. Pu, X. Lu, Y. Ning, L. Zhang, B. Wang, Z. Chen, P. Lv, Y. Yang, Z. Wang, Innovative binary $Na_{0.5}Bi_{0.5}TiO_3$-based composite ceramics with excellent comprehensive energy storage performances under low electric fields. Compos. Part. B: Eng. 288 (2025). http://dx.doi.org/10.1016/j.compositesb.2024.111853
10. Y. Pan, Q. Dong, J. Huang, Y. Zhang, X. Chen, X. Li, L. Deng, H. Zhou, Multi-scale enhanced energy storage performance in $Sm(Mg_{0.5}Sn_{0.5})O_3$-modified $Bi_{0.47}Na_{0.47}Ba_{0.06}TiO_3$ ceramics with a composite structure. J. Mater. Chem. A **13**(5), 3749–3764 (2025). http://dx.doi.org/10.1039/d4ta07670b
11. S. Li, K. Ma, Y. Ye, W. Han, S. Li, Y. Shi, Y. Tang, G. Cheng, X. Zhu, J. Qi, Effect of annealing temperature on optical properties of Erbium doped $Y_2Zr_2O_7$ transparent ceramics. Ceram. Int. **48**(24) (2022). http://dx.doi.org/10.1016/j.ceramint.2022.08.294
12. J. Wang, S. Hui, R. Guo, X. Sun, J. Bai, H. Xu, Z. Gong, C. Zheng, G. Shi, X. Lv, Effect of $Y_2Zr_2O_7$ content on improving mechanical properties and thermal shock resistance of AlN-based composite ceramics. Ceram. Int. **50**(17) (2024). http://dx.doi.org/10.1016/j.ceramint.2024.05.226
13. P. Mowe, F. Pfeiffer, O. Maus, W.G. Zeier, M. Winter, K. Neuhaus, Relationship between structure and room-temperature charge transport in highly acceptor-doped ceria and zirconia. Solid State Ionics. **428** (2025). http://dx.doi.org/10.1016/j.ssi.2025.116955
14. K. Lu, Y. Ye, W. Han, C. Zhang, L. Liang, H. Yuan, Y. Shi, J. Qi, T. Lu, Defect Regulation of Terbium-Doped $Y_2Zr_2O_7$ Transparent Ceramic for Wide-Range Multimode Tunable Light-Shielding Windows. J. Phys. Chem. Lett. **13**(34) (2022). http://dx.doi.org/10.1021/acs.jpclett.2c02177
15. J. Wang, K. Lu, Y. Ye, Y. Qin, W. Han, J. Qi, Samarium doped yttrium zirconate transparent ceramics for highly transparent reddish-orange light emitting applications. Ceram. Int. **48**(23) (2022). http://dx.doi.org/10.1016/j.ceramint.2022.08.094
16. Y. Ye, K. Lu, J. Qi, Developing Smart Temperature Sensing Window Based on Highly Transparent Rare-Earth Doped Yttrium Zirconate Ceramics, ACS Appl. Mater. Interfaces. **14**(34) (2022). http://dx.doi.org/10.1021/acsami.2c11404

17. K. Lu, W. Han, G. Cheng, X. Zhu, S. Li, H. Guo, B. Gu, Y. Ye, J. Qi, T. Lu, Dy^{3+}-doped $Y_2Zr_2O_7$ highly transparent ceramics for ultraviolet excitable warm white light-emitting applications. J. Am. Ceram. Soc. **106**(6) (2023). http://dx.doi.org/10.1111/jace.19059
18. K. Lu, M. Guan, Y. Xie, W. Han, Y. Ye, Z. Li, G. Wang, J. Qi, T. Lu, Achieving Efficient Optical Thermometry in Terbium-Doped Highly Transparent Ceramics. Adv. Opt. Mater. **12**(18) (2024). http://dx.doi.org/10.1002/adom.202400110
19. X. Wang, H. Sun, M. Wang, M. Tang, Y. Lan, R. Xu, Y. Feng, Z. Li, X. Wei, Z. Xu, Low-temperature sintering of PLSZT-based antiferroelectric ceramics in reducing atmosphere for energy storage. J. Eur. Ceram. Soc. **44**(2), 898–906 (2024). http://dx.doi.org/10.1016/j.jeurceramsoc.2023.09.053
20. L. Wang, W. Cao, C. Liang, C. Wang, H. Zhao, C. Wang, Excellent energy-storage performance in BNT-BT lead-free ceramics through optimized electromechanical breakdown. Mater. Today Phys. **47** (2024). http://dx.doi.org/10.1016/j.mtphys.2024.101545
21. Q. Zheng, B. Xie, Y. Tian, Q. Wang, H. Luo, Z. Liu, H. Zhang, High recoverable energy density of $Na_{0.5}Bi_{0.5}TiO_3$-based ceramics by multi-scale insulation regulation and relaxor optimization strategy. J. Materiomics. **10**(4), 845–856 (2024). http://dx.doi.org/10.1016/j.jmat.2023.10.005
22. C. Long, Z. Su, A. Xu, H. Huang, L. Liu, L. Gu, W. Ren, H. Wu, X. Ding, $Bi_{0.5}Na_{0.5}TiO_3$-based energy storage ceramics with excellent comprehensive performance by constructing dynamic nanoscale domains and high intrinsic breakdown strength. Nano Energy. 124 (2024). http://dx.doi.org/10.1016/j.nanoen.2024.109493
23. T. Deng, Z. Liu, T. Hu, K. Dai, Z. Hu, G. Wang, Excellent energy-storage performance in $Bi_{0.5}Na_{0.5}TiO_3$-based lead-free composite ceramics via introducing pyrochlore phase $Sm_2Ti_2O_7$. Chem. Eng. J. 465 (2023). http://dx.doi.org/10.1016/j.cej.2023.142992
24. Q. Chen, H. Chen, D. Wang, T. Gao, Q. Li, R. Lang, Z. Tan, J. Xing, J. Zhu, Superior energy storage properties with prominent thermal stability in lead-free KNN-based ceramics through multi-component optimization strategy. Chem. Eng. J. 494 (2024). http://dx.doi.org/10.1016/j.cej.2024.152823
25. H. Li, X. Li, Y. Du, X. Chen, H. Qin, Y. Tabak, A. Evcin, F. Hussain, K. Song, H. Zhou, J. Zhao, D. Wang, Remarkable energy storage performance of $BiFeO_3$-based high-entropy lead-free ceramics and multilayers. Chem. Eng. J. 499 (2024). http://dx.doi.org/10.1016/j.cej.2024.156112
26. C. Li, M. Yao, X. Yao, An effective strategy for enhancing energy storage density in $(Pb_{1-1.5x}Gd_x)(Zr_{0.87}Sn_{0.12}Ti_{0.01})O_3$ antiferroelectric ceramics. J. Mater. Chem. A **11**(35), 18689–18701 (2023). http://dx.doi.org/10.1039/d3ta03491g
27. J. Wang, S. Zhang, L. Yang, G. He, Z. Hu, Enhancing the energy storage performance of NBT-based ceramics through grain boundary design. Ceram. Int. **51**(18), 25094–25102 (2025). http://dx.doi.org/10.1016/j.ceramint.2025.03.191
28. D. Li, D. Xu, W. Zhao, M. Avdeev, H. Jing, Y. Guo, T. Zhou, W. Liu, D. Wang, D. Zhou, A high-temperature performing and near-zero energy loss lead-free ceramic capacitor. Energy Environ. Sci. **16**(10),

4511–4521 (2023). http://dx.doi.org/10.1039/d3ee01545a

29. M. Khondabi, H. Ahmadvand, M. Javanbakht, Revisiting the Dielectric Breakdown in a Polycrystalline Ferroelectric: A Phase-Field Simulation Study. Adv. Theory Simul. **6**(1) (2022). http://dx.doi.org/10.1002/adts.202200314
30. Y. Li, M.Y. Tang, Z.G. Zhang, Q. Li, J.L. Li, Z. Xu, G. Liu, F. Li, $BaTiO_3$-based ceramics with high energy storage density. Rare Met. **42**(4), 1261–1273 (2023). http://dx.doi.org/10.1007/s12598-022-02175-y
31. S. Wang, J. Qian, G. Ge, F. Zhang, F. Yan, J. Lin, L. Tang, M. Yang, Z. Pan, X. Wei, B. Shen, Z. Liu, J. Zhai, Embedding Plate-Like Pyrochlore in Perovskite Phase to Enhance Energy Storage Performance of BNT-Based Ceramic Capacitors. Adv. Energy Mater. **15**(12) (2024). http://dx.doi.org/10.1002/aenm.202403926
32. N. Luo, X. He, C. Xu, Z. Chen, K. Zhao, Z. Cen, X. Chen, D. Shan, Y. Liu, Z. Liu, H. Xie, Y. Zhu, H. Huang, J.F. Li, S. Zhang, Ordering-Structured Antiferroelectric Composite Ceramics for Energy Storage Applications. Adv. Mater. **37**(11) (2025). http://dx.doi.org/10.1002/adma.202420258
33. F. Yang, Y. Bao, B. Zeng, J. Wu, X. Li, Y. Sun, Y. Chen, G. Wang, Excellent energy storage properties in ZrO_2 toughened $Ba_{0.55}Sr_{0.45}TiO_3$-based relaxor ferroelectric ceramics via multi-scale synergic regulation. Chem. Eng. J. **493** (2024). http://dx.doi.org/10.1016/j.cej.2024.152624
34. X. Li, Z. Dai, X. Li, C. Liu, Y. Zheng, Y. Zhang, S. Gu, X. Ren, Dual-doping strategy for enhancement of energy storage properties in $Bi_{0.5}Na_{0.5}TiO_3$-based ceramics. J. Alloys Compd. **1048** (2025). http://dx.doi.org/10.1016/j.jallcom.2025.185245
35. R.T. Parayil, S.K. Gupta, K. Sudarshan, B.S. Naidu, G.D. Patra, M. Mohapatra, Tweaking the structure and symmetry of $Y_2B_2O_7$:Eu^{3+} by B-site engineering for efficient and thermally stable phosphor: $Y_2Zr_2O_7$ versus $Y_2Ge_2O_7$. Mater. Res. Bull. 180 (2024). http://dx.doi.org/10.1016/j.materresbull.2024.113039
36. R. Xue, X. Liu, Y. Yang, X. Zhu, H. Wang, Enhanced energy storage density and efficiency in A/B-site-engineered silver niobate ceramics. Ceram. Int. **51**(23), 39549–39557 (2025). http://dx.doi.org/10.1016/j.ceramint.2025.06.190
37. X. Xiong, H. Liu, J. Zhang, L.L. da Silva, Z. Sheng, Y. Yao, G. Wang, M. Hinterstein, S. Zhang, J. Chen, Ultrahigh Energy-Storage in Dual-Phase Relaxor Ferroelectric Ceramics. Adv. Mater. **36**(48) (2024). http://dx.doi.org/10.1002/adma.202410088
38. D. Li, D. Zhou, D. Wang, W. Zhao, Y. Guo, Z. Shi, T. Zhou, S.K. Sun, C. Singh, S. Trukhanov, A.S.B. Sombra, Lead-Free Relaxor Ferroelectric Ceramics with Ultrahigh Energy Storage Densities via Polymorphic Polar Nanoregions Design. Small. **19**(8) (2022). http://dx.doi.org/10.1002/smll.202206958
39. H.-. Lian, M. Shi, S. Lv, L.-. Liu, X.-. Chen, Dielectric, ferroelectric, and energy storage properties of BNBTA-*x*SLZT lead-free ceramics. J. Eur. Ceram. Soc. **45**(6), 117219 (2025). http://dx.doi.org/10.1016/j.jeurceramsoc.2025.117219

40. C. Wang, J. Hao, L. Duan, D. Zhao, Y. Ma, J. Zhang, P. Ma, D. Han, F. Meng, Energy storage performance with ultrahigh energy density and power density of $Ba_{0.85}Ca_{0.15}Zr_{0.1}Ti_{0.9}O_3$-based lead-free ceramics through synergistic optimization. Ceram. Int. **51**(21), 35133–35143 (2025). http://dx.doi.org/10.1016/j.ceramint.2025.05.237
41. C. Liu, Z. Dai, Y. Zheng, X. Li, R. Dai, Y. Liu, W. Liu, S. Zhou, S. Gu, M. Fang, X. Ren, Simultaneous enhancement of the energy storage, transparency, and hardness properties of $K_{0.5}Na_{0.5}NbO_3$-based ceramics via a synergistic optimization strategy. J. Mater. Chem. A **47**, 41365–41374 (2025). http://dx.doi.org/10.1039/d5ta06456b
42. K. Ma, J. Cui, J. Li, X. Zhang, X. Han, L. Dong, P. Li, L. Wu, X. Qi, Multiple collaborative optimization strategy regulates tungsten bronze ceramics to achieve efficient energy storage performance. J. Energy Storage. **134**, 118203 (2025). http://dx.doi.org/10.1016/j.est.2025.118203

Figures

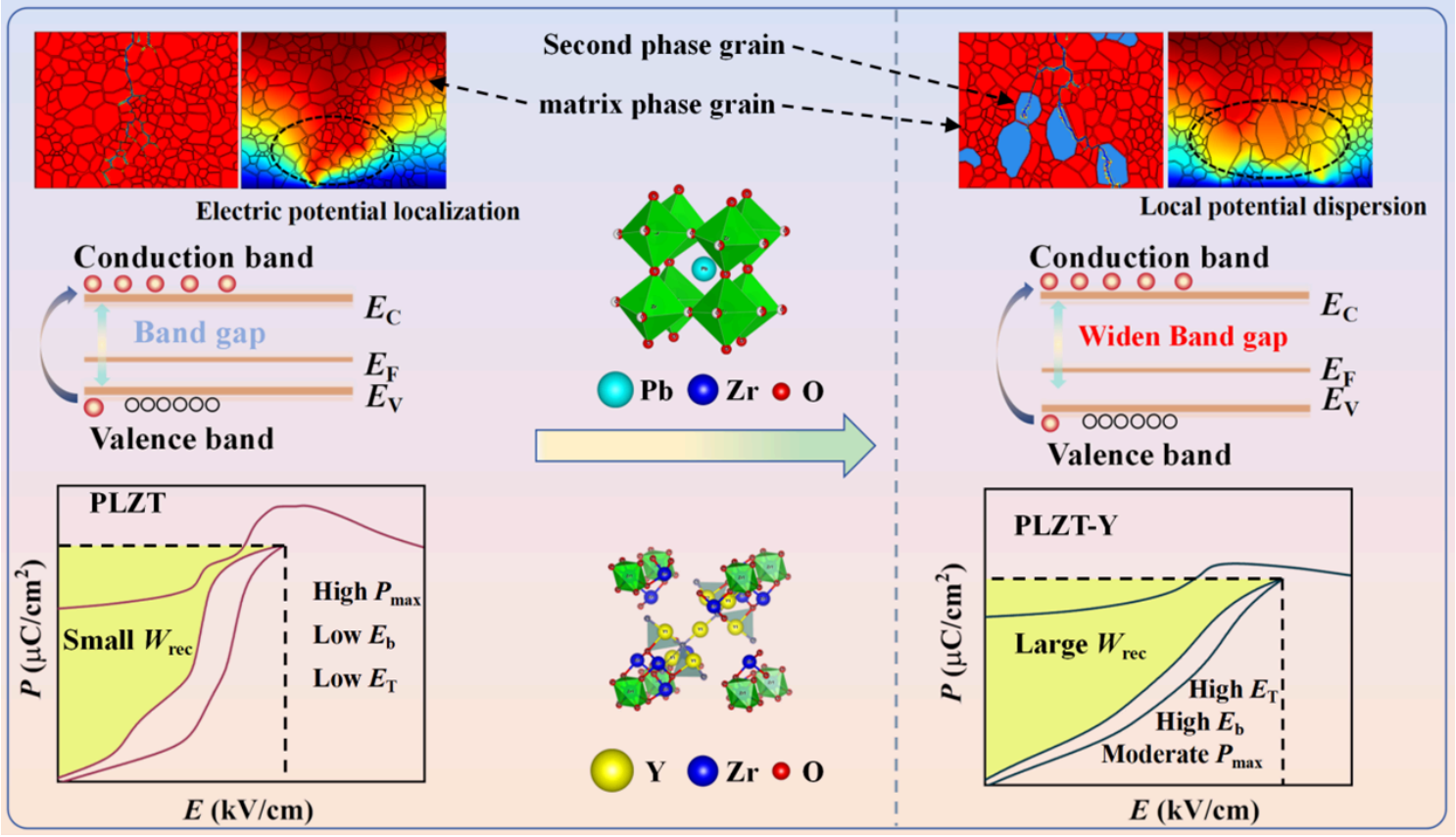


Figure 1

Schematic diagram of strategies for improving the comprehensive ESPs of PLZT by constructing composite ceramics

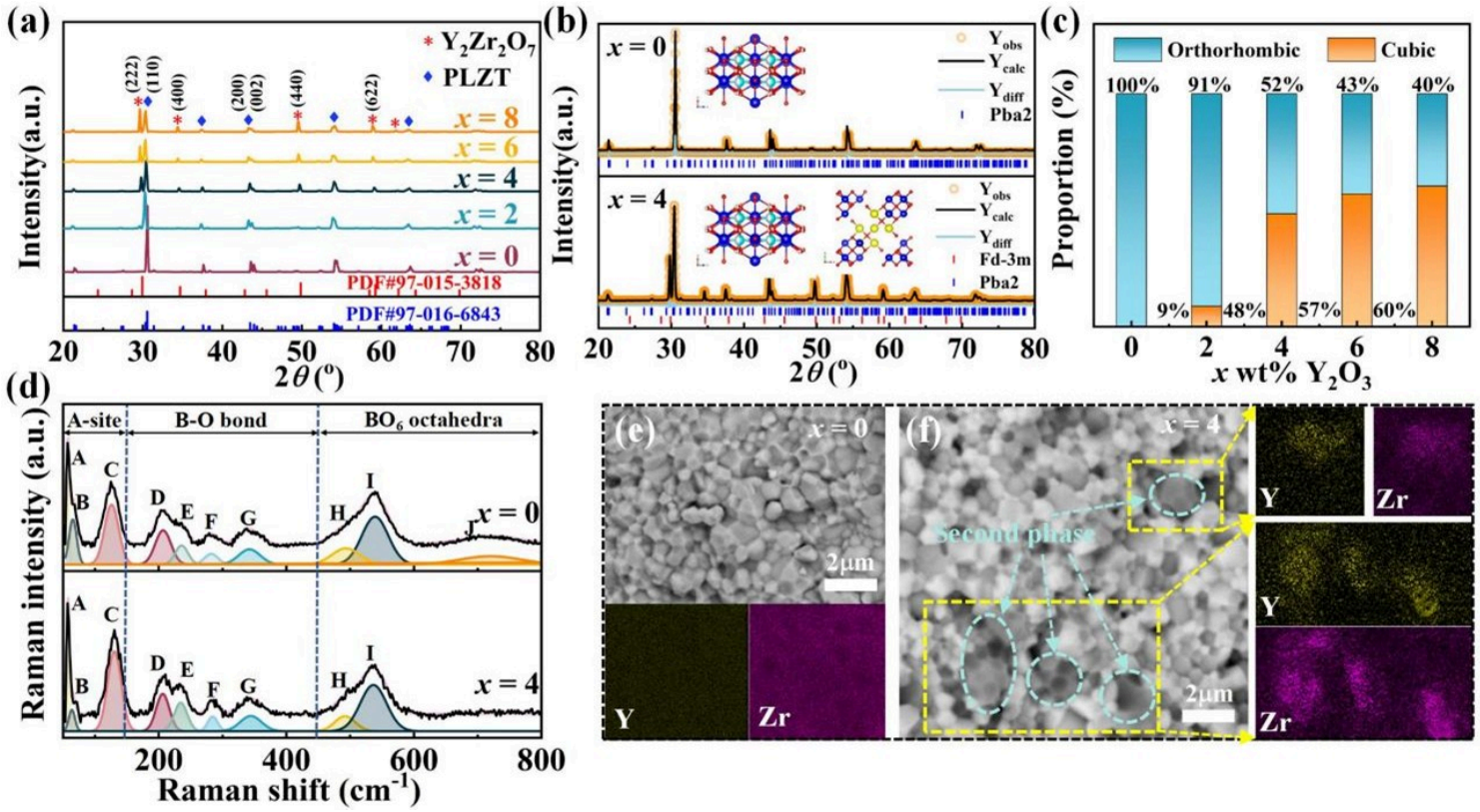


Figure 2

(a) XRD pattern of PLZT-*x* wt%Y_2O_3 ceramics; (b) The Rietveld refinement XRD patterns of Y0 and Y4 over 20^o to 80^o; (c) Phase proportion of PLZT-*x* wt% Y_2O_3 ceramics; (d) Raman spectra of Y0 and Y4 ceramics at room temperature; (e) BSE image and EDS image of Y0 ceramics; (f) BSE image and EDS image of Y4 ceramics.

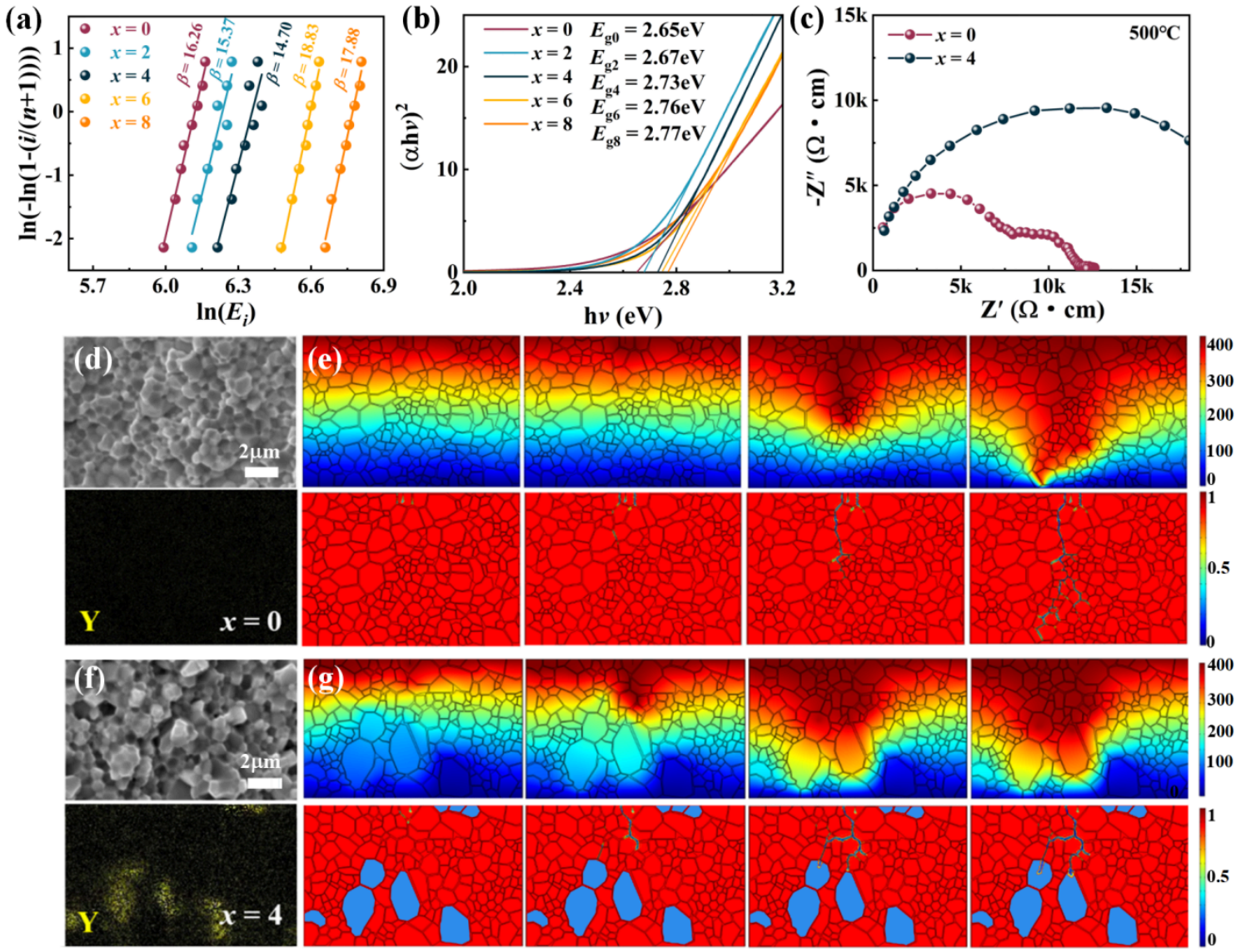


Figure 3

(a) Weibull distribution of E_b for PLZT- x wt% Y_2O_3 ceramics; (b) Tauc plot of PLZT- x wt% Y_2O_3 ceramics; (c) Impedance diagrams of Y0 and Y4 ceramics; (d) and (e) BSE image and EDS image of Y0 and Y4 ceramics; (f) and (g) Analog diagrams of Y4 ceramics.

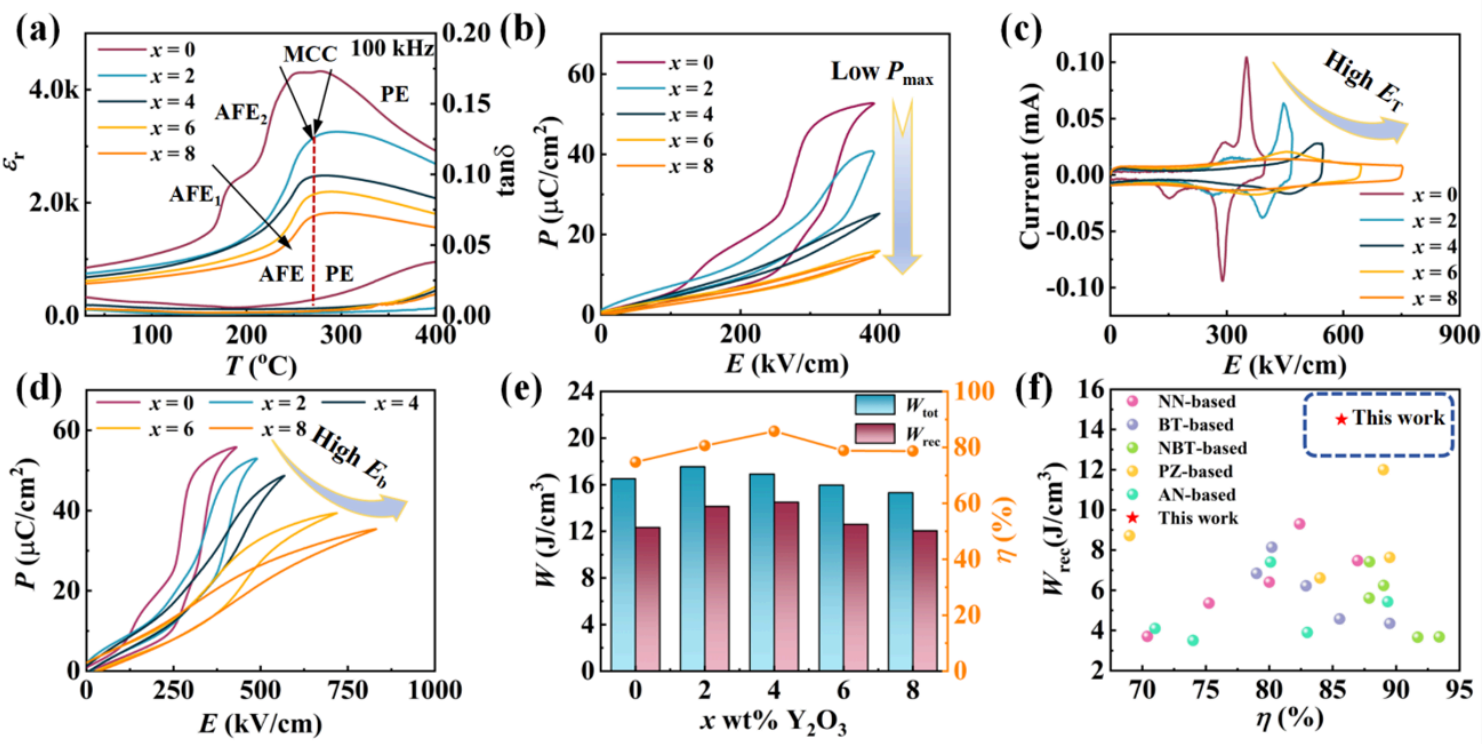


Figure 4

(a) dielectric temperature spectra of PLZT- *x* wt% Y_2O_3 ceramics; (b) *P-E* loops of PLZT- *x* wt% Y_2O_3 ceramics under the same electric field; (c) *I-E* loops of PLZT- *x* wt% Y_2O_3 ceramics at E_b; (d) *P-E* loops of PLZT- *x* wt% Y_2O_3 ceramics at E_b; (e) Comparison of W_{tot}, W_{rec} and *h* of PLZT- *x* wt% Y_2O_3 ceramics; (f) Comparison of P_{max}, P_r and ΔP for PLZT- *x* wt% Y_2O_3 ceramics.

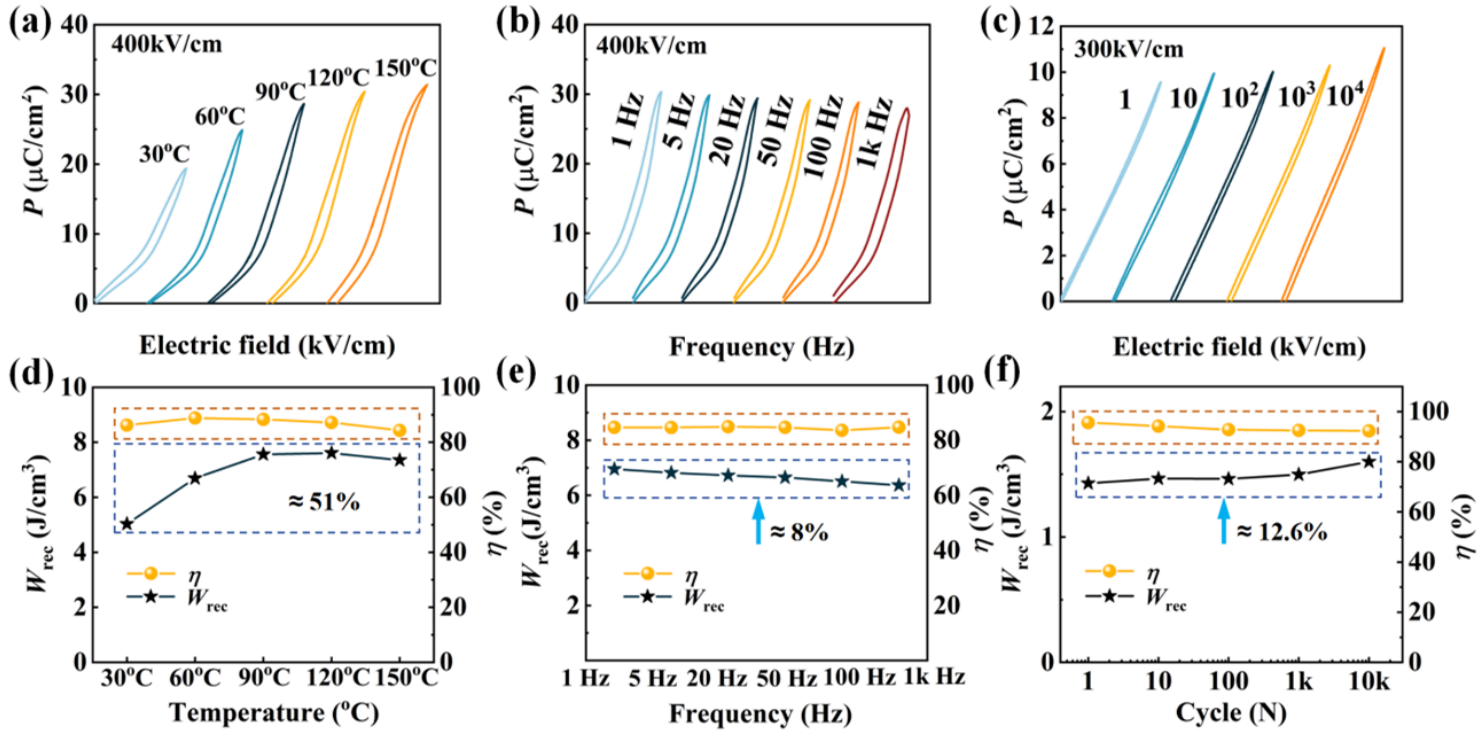


Figure 5

(a) *P-E* loops of Y4 ceramics at different temperatures at 400kV/cm and variations in W_{rec} and h with temperature; (b) *P-E* loops of Y4 ceramics at different frequencies under 400 kV/cm conditions and variations of W_{rec} and h with frequency; (c) *P-E* loops of Y4 ceramics at 300 kV/cm with different cycles and variations of W_{rec} and h with cycles.

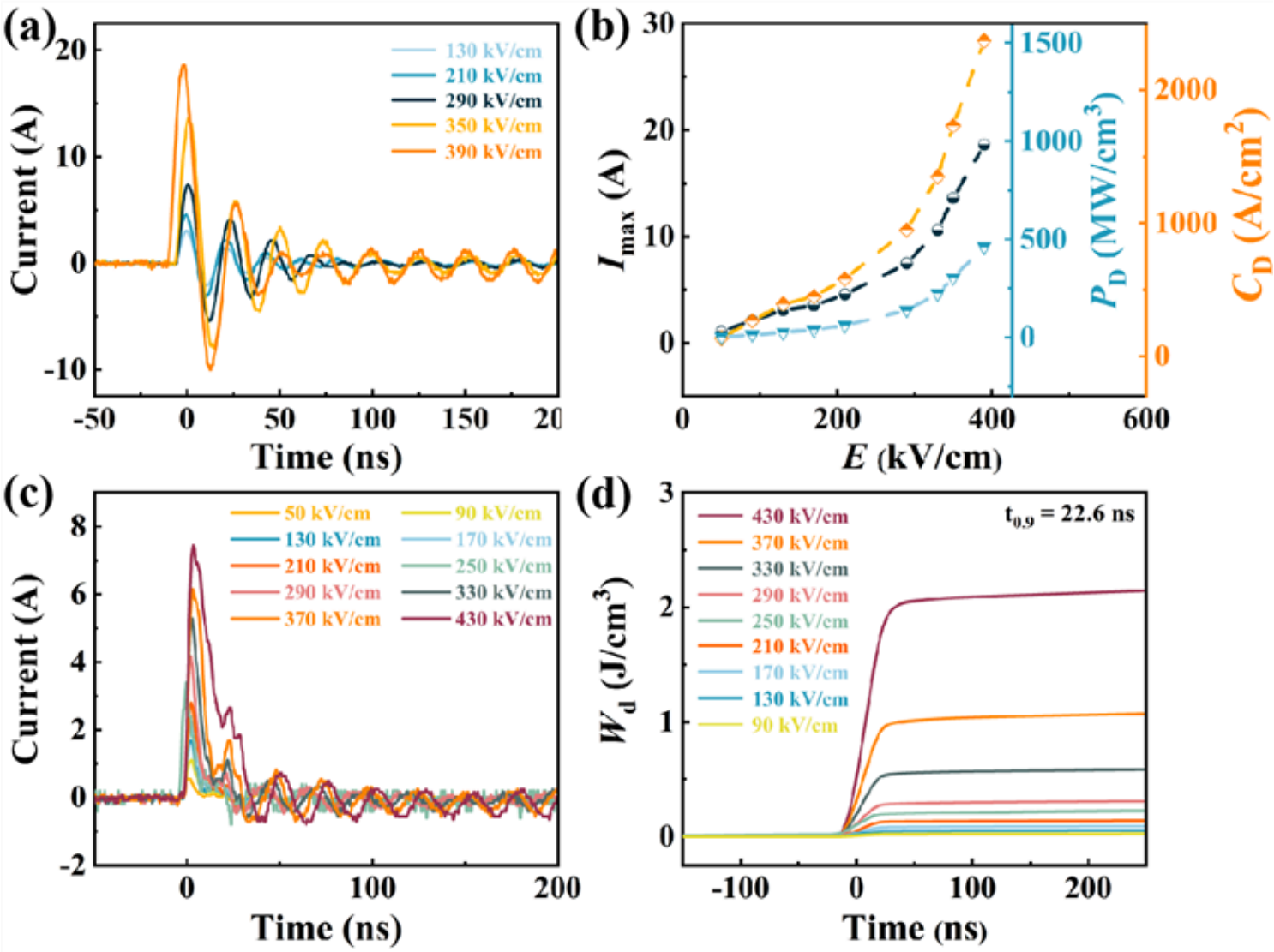


Figure 6

(a) Pulse charge-discharge performance of Y4 ceramic under different electric fields in the underdamped state; (b) Y4 ceramic I_{max}, P_D, C_D tests; (c) Pulse charge-discharge performance of Y4 ceramic under different electric fields in overdamped state; (d) Calculate the variation of W_d and $t_{0.9}$ over time by integration

Supplementary Files

This is a list of supplementary files associated with this preprint. Click to download.

- SupportingInformation.docx